IOP Publishing Smart Materials and Structures
Smart Mater. Struct. 25 (2016) 105007 (15pp) doi:10.1088/0964-1726/25/10/105007

Electrohydroelastic Euler–Bernoulli–Morison model for underwater resonant actuation of macro-fiber composite piezoelectric cantilevers

S Shahab[1] and A Erturk[2]

[1] Department of Biomedical Engineering and Mechanics, Virginia Polytechnic Institute and State University, Blacksburg, VA 24061, USA
[2] G W Woodruff School of Mechanical Engineering, Georgia Institute of Technology, Atlanta, GA 30332, USA

E-mail: alper.erturk@me.gatech.edu

Received 25 April 2016, revised 4 August 2016
Accepted for publication 23 August 2016
Published 16 September 2016

Abstract

Bio-inspired hydrodynamic thrust generation using smart materials has received growing attention over the past few years to enable improved maneuverability and agility, small form factor, reduced power consumption, and ease of fabrication in next-generation aquatic swimmers. In order to develop a high-fidelity model to predict the electrohydroelastic dynamics of macro-fiber composite (MFC) piezoelectric structures, in this work, mixing rules-based (i.e. rule of mixtures) electroelastic mechanics formulation is coupled with the global electroelastic dynamics based on the Euler–Bernoulli kinematics and nonlinear fluid loading based on Morison's semi-empirical model. The focus is placed on the dynamic actuation problem for the first two bending vibration modes under geometrically and materially linear, hydrodynamically nonlinear behavior. The electroelastic and dielectric properties of a representative volume element (piezoelectric fiber and epoxy matrix) between two subsequent interdigitated electrodes are correlated to homogenized parameters of MFC bimorphs and validated for a set of MFCs that have the same overhang length but different widths. Following this process of electroelastic model development and validation, underwater actuation experiments are conducted for different length-to-width aspect ratios (L/b) in quiescent water, and the empirical drag and inertia coefficients are extracted from Morison's equation to establish the electrohydroelastic model. The repeatability of these empirical coefficients is demonstrated for experiments conducted using aluminum cantilevers of different aspect ratios with a focus on the first two bending modes. The convergence of the nonlinear electrohydroelastic Euler–Bernoulli–Morison model to its hydrodynamically linear counterpart for increased L/b values is also reported. The proposed model, its harmonic balance analysis, and experimental results can be used not only for underwater piezoelectric actuation, but also for sensing and energy harvesting problems.

Keywords: piezoelectricity, actuation, vibration, underwater, macro-fiber composites, bio-inspired, morphing

(Some figures may appear in colour only in the online journal)

1. Introduction

Bio-inspired underwater vehicles have received growing interest over the last few years. As an alternative to conventional underwater vehicles with propeller-based propulsion systems, the motivation for using bio-inspired structures in aquatic locomotion is to enable enhanced low-speed maneuverability, silent operation, signature reduction, and reduced power consumption [1].

The applications of fish-like biomimetic locomotion range from underwater sensing and exploration for sustainable ecology to drug delivery and disease screening in medicine [1–3].

Various successful designs with motors and appropriate linkage systems or mechanisms have been proposed to mimic biological creatures in the existing literature [3, 4]. In these concepts, the locomotion is typically obtained by creating an undulatory motion in the tail portion connected to a passive caudal fin [4–6]. Other studies employing motor-based actuation include pectoral fins for locomotion [7, 8]. Although motor-based biomimetic vehicles have relatively high swimming speeds, they are often noisy and not easy to miniaturize. To overcome this problem, various research groups have explored the use of smart materials as actuators in bio-inspired aquatic robotics especially in the last few years [2].

The commonly used smart material actuators in bio-inspired applications are ionic polymer-metal composites (IPMCs), shape memory alloys, and piezoelectric materials as covered in a recent review article [2]. Among these three smart material types, the compliant IPMC technology offers the largest mechanical deformation for low voltage actuation, making it arguably the most heavily researched smart material in bio-inspired underwater actuation and aquatic robotics applications. The main tradeoff in the use of IPMCs is the resulting low actuation force in contrast to their large geometric deformation capabilities. Several studies have been conducted by actuating a tail embedded with IPMC, such as a cantilever beam, with or without a passive caudal fin attached, including tadpole like robot in undulatory motion [9], an untethered swimming robot [10], among other centimeter-scale examples [11, 12]. This type of locomotion created by IPMCs has been modeled by several authors [13–16].

Unlike conventional piezoelectric actuators, the macro-fiber composite (MFC) piezoelectric technology developed at the NASA Langley Research Center [17, 18] in the last decade (and subsequently commercialized by the Smart Material Corp.) offers flexible and robust piezoelectric actuators made from PZT (lead zirconate titanate) fibers and epoxy matrix sandwiched between interdigitated electrodes and assembled in Kapton (figure 1). These actuators offer significant advantages over monolithic piezoceramic materials which have limitations such as their brittle nature and low allowable curvature. The MFC technology provides high strain and stress performance based on the 33-mode of piezoelectricity (i.e. electric field and strain are in the same direction), flexibility, endurance, and they can be manufactured in various sizes [17, 18] along with relatively hydrophobic behavior with polyester electrode sheets. Furthermore, the MFCs use PZT fibers with rectangular cross section, yielding dramatically enhanced electrode contact and reduced dielectric loss as compared to their previous generation counterparts, such as the active fiber composites with circular cross section [19]. Therefore the MFCs overcome the problem of small displacement response associated with piezoelectric actuators without substantially compromising high actuation force capability. MFC actuators have been successfully used in tethered underwater robotic fish [20–22] and lately being applied for active control and hydrodynamic

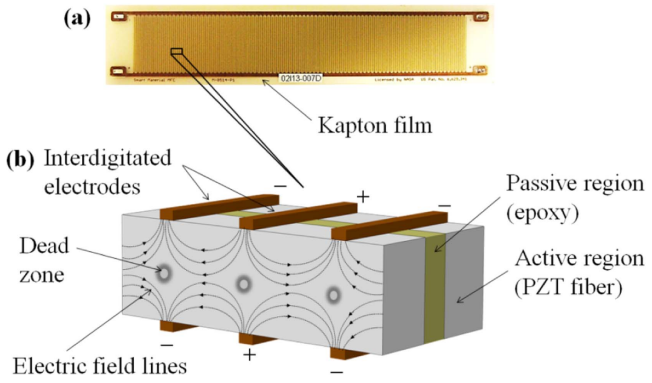

Figure 1. (a) Picture of an MFC laminate and (b) close-up 3D representation showing PZT fibers, epoxy matrix, and interdigitated electrodes with non-uniform electric field lines (the composite structure is embedded in Kapton film for robustness).

performance enhancement of flexible fins actuated in an unsteady fluid flow [23]. Erturk and Delporte [24] investigated underwater thrust and power production using MFC bimorphs with and without a passive caudal fin extension (with a focus on the first two vibration modes). More recently, an untethered piezoelectric robotic fish was developed and a swimming speed of 0.3 body length/second was reported by Cen and Erturk [25].

Erturk and Delporte [24] performed in-air and underwater base excitation experiments of an MFC-based fish-like propulsor with a caudal fin for energy harvesting. Comparing the in-air and underwater test results showed that maximum underwater power output is an order of magnitude larger than its in-air counterpart for the same base acceleration level due to fluid loading effects. More recently electrohydroelastic dynamics of a fully submerged MFC bimorph propulsor was investigated by Cen and Erturk [25] for the modeling and experimental analysis of fish-like aquatic robotics by accounting the hydrodynamic effects following the work by Sader and others [26–29]. Likewise, for underwater purposes, Brunetto *et al* [30], Mbemmo *et al* [13], and Aureli *et al* [14] used similar approaches to analyze the dynamics of IPMC samples. Analyzing the force exerted on the oscillating structure by the fluid shows that the fluid effects can be taken as added mass and hydrodynamic damping [13, 14, 24–32]. The hydrodynamic effects reduce the resonance frequencies of the structure and increase the damping ratios as compared to in-air resonance frequencies and damping ratios.

The linear hydrodynamic function developed based on Sader's theory [26–29] assumes infinitesimal vibration amplitude and large length-to-width (L/b) aspect ratio. Therefore, as the vibration amplitude increases or L/b ratio decreases, Sader's model fails to be accurate. Through extending the approach proposed by Tuck [33] and Sader [26], studies were performed by Aureli *et al* [16, 34], Falcucci *et al* [35], Phan *et al* [36], and Tafuni and Sahin [37] to introduce a correction to Sader's hydrodynamic function by accounting for nonlinear hydrodynamic effects. The goal was to develop accurate models for predicting underwater response of flexible beams for a broad range of frequencies

and aspect ratios and in some cases for relatively large amplitude vibrations. Aureli *et al* [34] and Phan *et al* [36] performed computational fluid dynamics analysis to understand the effects of certain parameters on the vibration of a submerged beam and to obtain a hydrodynamic correction term added to the classical hydrodynamic function. Facci and Porfiri [38] performed numerical investigation on the 3D fluid flow field induced by vibration of cantilevered beams with different aspect ratios. In that work [38], model simulations showed that the hydrodynamic function given by Sader [26], Bidkar *et al* [39] and Aureli *et al* [34] predicted the distributed load experienced by oscillating beams for $L/b > 3$ with reasonable accuracy. As the aspect ratio of the beam decreased, the 3D fluid effects were responsible for significant difference in the distributed added mass loading due to vortex shedding from the edges of the beam [38, 40] while the actual loads are overestimated by these theories [26, 34]. However, the modeling approach proposed by Aureli *et al* [34] was found to be effective in predicting hydrodynamic damping for a broad range of aspect ratios. Cha *et al* [31] and Kopman and Porfiri [41] adapted Morison's nonlinear equation [42–45] to incorporate the effects of the surrounding fluid on the oscillating beams with small aspect ratios. Morison's equation was used to calculate the fluid loading on a circular cylinder in viscous oscillatory flow consisting of added mass and nonlinear damping as functions of the transverse motion of the cantilever beam.

In this work, we explore underwater electrohydroelastic dynamic actuation of MFC bimorph cantilevers with interdigitated electrodes for different L/b aspect ratios in a quiescent fluid [46, 47]. The electroelastic model that bridges the mixing rules (i.e. rule of mixtures) formulation and global resonant dynamics of the composite is coupled with hydrodynamic effects from Morison's nonlinear equation. The hydrodynamic coefficients (inertia and drag coefficients) in Morison's equation are extracted experimentally for MFC cantilevers with three aspect ratios and the resulting nonlinear mathematical framework is explored by using the method of harmonic balance. The dependence of the experimentally extracted hydrodynamic coefficients on the L/b aspect ratio is shown and compared with the results reported in literature. Specifically, the aspect-ratio dependent hydrodynamic coefficients from base-excited aluminum beams are identified in a separate set of experiments and used to predict the dynamics of the first two bending modes with good accuracy for MFC cantilevers with three aspect ratios. The dependence of the identified hydrodynamic inertia and drag coefficients on the Keulegan–Carpenter (KC) number [48] is also reported for the first two bending modes.

2. Electrohydroelastic dynamics of MFC bimorph cantilevers

2.1. MFC structure and mixing rules formulation

An MFC laminate and its interdigitated electrode configuration (which results in a complex electric field distribution) are shown in figures 2(a)–(c). The non-uniform electric field lines through the piezoelectric fibers and dead zones are depicted in figure 1(c). Because of the non-uniform electric field and heterogeneous complex structure involving active and passive regions (in figure 1(b); PZT fiber and epoxy, respectively) in MFCs, a straightforward integration cannot be performed to obtain the electromechanical coupling and capacitance parameters. This section briefly presents an analytical solution by combining the effective properties of a representative volume element (RVE—figure 2(d)) for an MFC laminate using the 33-mode of piezoelectricity (electric field and strain directions are coincident) prior to the distributed-parameter electroelastic model.

The mixing rules formulation [49, 50] is employed to homogenize the elastic and dielectric parameters of the MFCs. Specifically, effective elastic modulus, piezoelectric charge constant, and permittivity constant are incorporated in the distributed-parameter electroelastic model [51, 52]. The piezoelectric fibers and interdigitated electrodes are modeled as a set of piezoelectric RVEs in 33-mode (shown in figures 2(c) and (d)). Each RVE is connected in parallel to the remaining hundreds of RVEs along the length and width of the MFC laminate.

The linear constitutive equations for a piezoelectric thin beam (RVE in figure 2(d)) with 33-mode coupling are

$$T_3 = c^E_{33,e} S_3 - e_{33,e} E_3, \tag{1}$$

$$D_3 = e_{33,e} S_3 + \varepsilon^S_{33,e} E_3, \tag{2}$$

where T_3 is the stress, S_3 is the strain, E_3 is the electric field, D_3 is the electric displacement, $c^E_{33,e}$ is the equivalent elastic modulus at constant electric field, $e_{33,e}$ is the effective piezoelectric stress constant ($e_{33,e}$ can be given in terms of the more commonly used piezoelectric strain constant, $d_{33,e}$ as $e_{33,e} = d_{33,e} c^E_{33,e}$), and $\varepsilon^S_{33,e}$ is the permittivity component at constant strain, respectively (subscript e stands for equivalent properties). Analytical modal analysis of an Euler–Bernoulli beam with monolithic piezoelectric layers for closed-form distributed-parameter solutions has been thoroughly covered in previous efforts [53] for energy harvesting applications. For brevity, the key concepts will be developed and applied in this paper.

The equivalent elastic modulus ($c^E_{33,e}$), piezoelectric charge constant ($d_{33,e}$), and dielectric relative constant ($\varepsilon^S_{33,e}$) are obtained by using mixing rules as follows [49, 50]:

$$c^E_{33,e} = \nu c^E_{33,p} + (1 - \nu) c^E_{33,m}, \tag{3}$$

$$d_{33,e} = \frac{1}{c^E_{33,e}} \nu d_{33,p} c^E_{33,p}, \tag{4}$$

$$\varepsilon^S_{33,e} = [\nu \varepsilon^T_{33,p} + (1 - \nu) \varepsilon^T_{33,m}] - d^2_{33,e} c^E_{33,e}, \tag{5}$$

where ν is the PZT fiber volume fraction and is defined by the measurement done from the digital image of the planar surface of an MFC actuator (shown in figure 2(b)) and ε^T_{33} is the permittivity component at constant stress. The subscripts p and m stand for PZT fiber and matrix (epoxy) properties in RVE, respectively. The mixing rules-based effective

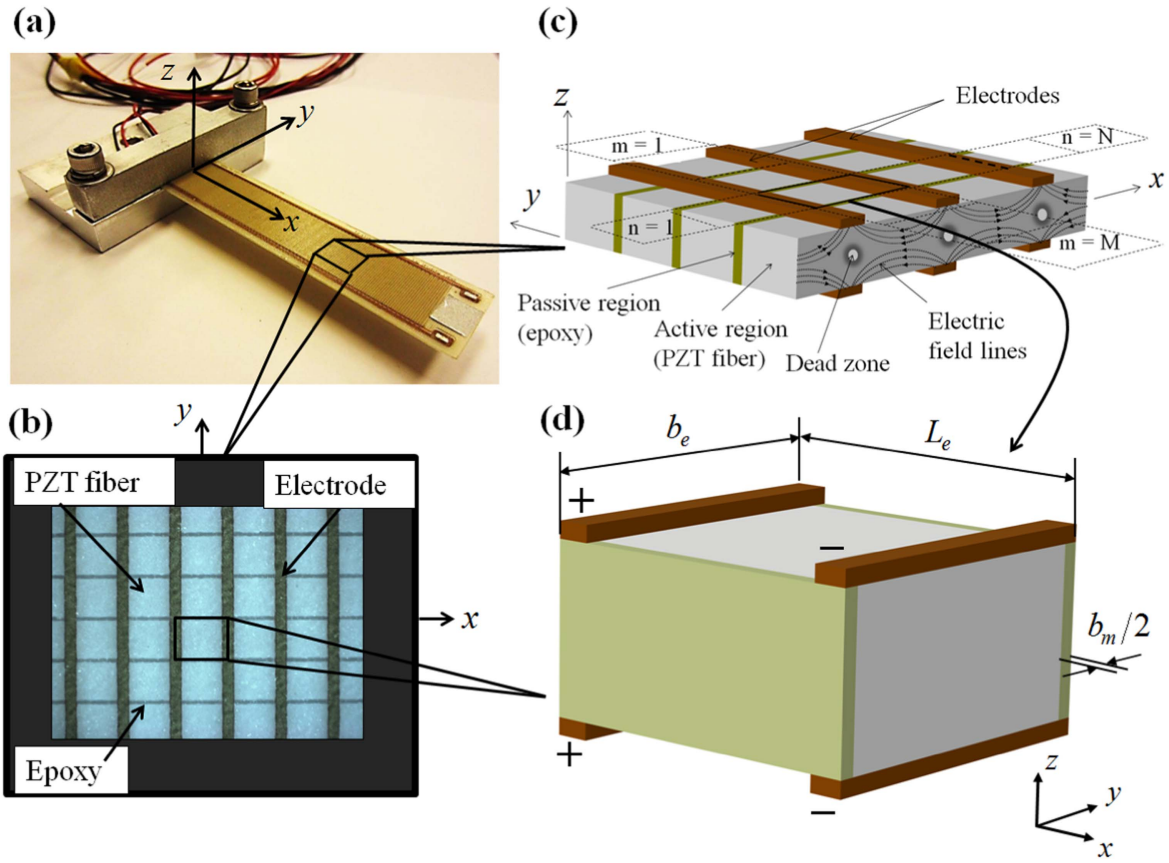

Figure 2. (a) MFC bimorph (made from two MFC laminates bonded using high-shear-strength epoxy); (b) digital image of the planar surface of an MFC actuator (M8514-P1 with polyester electrode sheets and approximately 90% volume fraction of PZT fibers) under optical microscope; (c) schematic view showing the interdigitated electrodes and non-uniform electric field lines and (d) a representative volume element that operates in the 33-mode of piezoelectricity.

electroelastic parameters will be coupled with the global electroelastic dynamics based on the Euler–Bernoulli kinematics in the next section for an MFC bimorph using 33-mode of piezoelectricity in bending operation.

2.2. In vacuo coupled mechanical and electrical circuit equations

Electroelastically coupled equations for in vacuo actuation of an MFC cantilever bimorph (figure 3) for small amplitude bending vibrations and linearized piezoelectricity can be obtained as follows[3]

$$D\frac{\partial^4 w(x,t)}{\partial x^4} + c_\alpha \frac{\partial^5 w(x,t)}{\partial x^4 \partial t} + c_\beta \frac{\partial w(x,t)}{\partial t} + m_s \frac{\partial^2 w(x,t)}{\partial t^2} = \vartheta \left[\frac{\mathrm{d}\delta(x)}{\mathrm{d}x} - \frac{\mathrm{d}\delta(x-L)}{\mathrm{d}x}\right] v(t), \tag{6}$$

$$-i(t) + C_p \frac{\mathrm{d}v(t)}{\mathrm{d}t} + \vartheta \int_0^L \frac{\partial^3 w(x,t)}{\partial x^2 \partial t}\,\mathrm{d}x = 0, \tag{7}$$

where D is the bending stiffness of the composite cross section, c_α is the stiffness-proportional damping coefficient, c_β is the mass-proportional damping coefficient[4], m_s is the mass per unit length of the beam, $L = L_a$ is the active overhang length, ϑ is the electromechanical coupling term, C_p is the capacitance, $\delta(x)$ is the Dirac delta function, $i(t)$ is the electrical current input (negative sign indicates current flow into the system), $v(t)$ is the actuation voltage input, and $w(x, t)$ is the transverse displacement on the reference surface (in z-direction). Note that this model assumes perfect bonding between the laminates of the bimorph structure, furthermore it neglects shear distortion or rotary inertia effects.

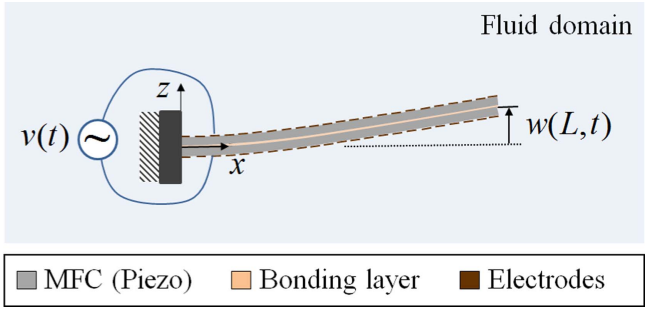

Figure 3. Schematic representation of a geometrically bimorph cantilever under dynamic actuation in an unbounded quiescent fluid domain.

[3] In the experiments of this paper, infinitesimal in-air vibration case will be used to approximate *in vacuo* condition so that hydrodynamic load can be superimposed as in the next section.

[4] This combined generalized proportional damping form is assumed to account for the internal losses as a convenient mathematical representation.

For the resulting bimorph MFC cantilever, the electromechanical coupling term, ϑ, and capacitance, C_p, are

$$\vartheta = Md_{33,e}c^{E}_{33,e}\frac{A_e}{L_e}h_{pc}, \tag{8}$$

$$C_p = MN\varepsilon^{S}_{33,e}\frac{A_e}{L_e}, \tag{9}$$

In each RVE (figure 2(d)), b_e is the sum of the width of piezoceramic fiber and matrix layer (epoxy), b_m, in the direction of bimorph width. In equation (8), M is the number of RVE in active width direction of the bimorph, b_a, as $b_a = Mb_e$. In equation (9), N is the number of RVE in active overhang length direction, L_a, as $L_a = NL_e$. L_e is the distance between two subsequent electrodes (center to center) in the direction of bimorph length, A_e is the effective cross sectional area, and h_{pc} is defined as the position of center of piezoceramic layer from the neutral axis (in thickness direction).

The transverse deflection of the reference surface at position x and time t is

$$w(x, t) = \sum_{r=1}^{\infty}\phi_r(x)\eta_r(t), \tag{10}$$

where $\phi_r(x)$ and $\eta_r(t)$ are the mass-normalized eigenfunction and the generalized modal coordinate for the rth mode, respectively. The eigenfunction denoted by $\phi_r(x)$ is given for the transverse vibration of a uniform clamped-free beam as

$$\phi_r(x) = \sqrt{\frac{1}{m_sL}}\left[\cos\frac{\lambda_r}{L}x - \cosh\frac{\lambda_r}{L}x + \frac{\sin\lambda_r - \sinh\lambda_r}{\cos\lambda_r + \cosh\lambda_r}\times\left(\sin\frac{\lambda_r}{L}x - \sinh\frac{\lambda_r}{L}x\right)\right], \tag{11}$$

where λ_r is the eigenvalue of the rth mode obtained from the characteristic equation

$$1 + \cos\lambda\cosh\lambda = 0, \tag{12}$$

The expression given for $\phi_r(x)$ satisfies the following orthogonality conditions [25]:

$$\int_0^L \phi_s(x)m_s\,\phi_r(x)\mathrm{d}x = \delta_{rs}, \tag{13}$$

$$\int_0^L \phi_s(x)\,D\frac{\mathrm{d}^4\phi_r(x)}{\mathrm{d}x^4}\mathrm{d}x = \omega_r{}^2\delta_{rs}, \tag{14}$$

where

$$\omega_r = \lambda_r^2\sqrt{D/m_sL^4}\,. \tag{15}$$

Here ω_r is the undamped natural frequency of the rth vibration mode and δ_{rs} is the Kronecker delta. For harmonic excitation of the form $v(t) = Ve^{j\omega t}$ (where ω is the excitation frequency and j is the unit imaginary number), assuming harmonic steady-state modal mechanical response $\eta_r(t) = H_re^{j\omega t}$ and current $i(t) = Ie^{j\omega t}$, using equation (10) in equations (6) and (7), multiplying by $\phi_s(x)$, and integrating over the length of the cantilever give the following equations for the complex amplitudes:

Table 1. Modal electromechanical coupling and equivalent capacitance of an MFC bimorph for the series and parallel connections of individual MFC single laminates.

	Series connection	Parallel connection
θ_r	$\vartheta\frac{\mathrm{d}\phi_r(x)}{\mathrm{d}x}\Big\vert_{x=L}$	$2\vartheta\frac{\mathrm{d}\phi_r(x)}{\mathrm{d}x}\Big\vert_{x=L}$
C^{eq}	$C_p/2$	$2C_p$

$$(\omega_r{}^2 - \omega^2 + j2\zeta_r\,\omega_r\omega)H_r = \theta_rV, \tag{16}$$

$$-I + j\omega C^{\mathrm{eq}}V + j\omega\sum_{r=1}^{\infty}\theta_rH_r = 0, \tag{17}$$

where θ_r is the modal electromechanical coupling, C^{eq} is the equivalent capacitance of the bimorph cantilever, and ζ_r is the modal mechanical damping ratio. The modal electromechanical coupling and equivalent capacitance depend on the way the MFC laminates are electrically connected. The analytical expressions for the equivalent capacitance and modal electromechanical coupling are given in table 1 for the series and parallel connections [53] of the MFC laminates.

Solving equations (16) and (17) for the displacement frequency response function (FRF), $\alpha(\omega, x)$, and the admittance FRF (current input per actuation voltage), $\beta(\omega)$, yields

$$\alpha(\omega, x) = \frac{w(x, t)}{Ve^{j\omega t}} = \sum_{r=1}^{\infty}\frac{\theta_r\phi_r(x)}{\omega_r{}^2 - \omega^2 + 2j\zeta_r\omega_r\omega}, \tag{18}$$

$$\beta(\omega) = \frac{I}{V} = j\omega\left(C^{\mathrm{eq}} + \sum_{r=1}^{\infty}\frac{\theta_r^2}{\omega_r{}^2 - \omega^2 + j2\zeta_r\,\omega_r\omega}\right). \tag{19}$$

The velocity FRF can be obtained through multiplying $\alpha(\omega, x)$ by $j\omega$ for harmonic response of the cantilever bimorph.

2.3. Combining the fluid load: electrohydroelastic dynamics of a bimorph cantilever

Electrohydroelastically coupled equations for underwater actuation of an MFC cantilever bimorph (figure 3) can be expressed as follows:

$$D\frac{\partial^4w(x, t)}{\partial x^4} + c_\alpha\frac{\partial^5w(x, t)}{\partial x^4\partial t} + c_\beta\frac{\partial w(x, t)}{\partial t} + m_s\frac{\partial^2w(x, t)}{\partial t^2} + \Gamma(x, t) = \vartheta\left[\frac{\mathrm{d}\delta(x)}{\mathrm{d}x} - \frac{\mathrm{d}\delta(x - L)}{\mathrm{d}x}\right]v(t), \tag{20}$$

$$-i(t) + C_p\frac{\mathrm{d}v(t)}{\mathrm{d}t} + \vartheta\int_0^L\frac{\partial^3w(x, t)}{\partial x^2\partial t}\,\mathrm{d}x = 0. \tag{21}$$

Here $\Gamma(x, t)$ is the hydrodynamic loading of the surrounding fluid per unit length ($L = L_o$ is the overall overhang length) and it is expressed by Morison's semi-empirical equation

as [42, 43]:

$$\Gamma(x,\,t) = \frac{\pi}{4}\rho_w b^2 c_m \frac{\partial^2 w(x,\,t)}{\partial t^2} + \frac{1}{2}\rho_w b c_d \frac{\partial w(x,\,t)}{\partial t}\left|\frac{\partial w(x,\,t)}{\partial t}\right|, \tag{22}$$

where ρ_w is the mass density of water and b is the overall width of the bimorph. Moreover, c_m and c_d are the inertia and drag coefficients, respectively, which depend on the aspect ratio and to be determined experimentally. Clearly, the damping component in Morison's equation introduces quadratic nonlinearity (different from the classical linearized hydrodynamic function presented by Sader [26]), therefore vibration modes need to be explored separately. The structural (geometric and material) behavior is assumed to be linear.

Assuming well separated modes, the transverse deflection of the reference surface at position x and time t can be expressed as

$$w(x,\,t) \cong \sum_{r=1}^{\infty} \phi_r(x)\eta_r(t), \tag{23}$$

where $\phi_r(x)$ and $\eta_r(t)$ are the respective eigenfunction (from the linear in-vacuo solution) and modal coordinate[5].

Substituting the expression for $w(x,\,t)$ into equations (20) and (21), multiplying by the mass normalized eigenfunction $\phi_s(x)$, integrating over the length of the beam, and applying the orthogonality conditions, one obtains

$$(1+\mu_r)\ddot{\eta}_r(t) + (2\zeta_r\omega_r + \gamma_r|\dot{\eta}_r(t)|)\dot{\eta}_r(t) + \omega_r^2\eta_r(t) = \theta_r v(t), \tag{24}$$

$$-i_r(t) + C^{\mathrm{eq}}v(t) + \theta_r\dot{\eta}_r(t) = 0, \tag{25}$$

where $\mu_r = (\pi/4)(\rho_w b^2 c_{mr}/m_s)$ and $\gamma_r = (1/2)\rho_w b c_{\mathrm{dr}} \int_0^L \phi_r^2(x)|\phi_r(x)|\mathrm{d}x$. Here c_{mr} and c_{dr} are the inertia and drag coefficients for the rth vibration mode.

We note that equation (24) has quadratic nonlinearity due to fluid damping. In this work, the method of harmonic balance is used to analyze periodic solutions of equations (24) and (25). Using this method, a Fourier series solution is assumed and the ordinary differential equations are replaced with algebraic equations (the details of harmonic balance analysis have been extensively explained elsewhere [54–58]). A single term (i.e. single harmonic) is deemed sufficient in this effort.

The unknown modal coordinate $\eta_r(t)$ is expressed as

$$\eta_r(t) = H_{0r}\cos\omega t + H_{1r}\sin\omega t. \tag{26}$$

The voltage, $v(t)$, and the current flow through the piezoelectric bimorph, $i_r(t)$, are of the form

$$v(t) = V\cos\omega t, \tag{27}$$

$$i_r(t) = I_{0r}\cos\omega t + I_{1r}\sin\omega t. \tag{28}$$

[5] Note that the assumption of modes being well separated is a reasonable one for bending vibration and it enables analyzing the individual bending modes separately to extract modal inertia and drag coefficients. Such an assumption would not be necessary in a totally numerical solution setting (although modal insight would not be clear in that case).

Substituting equations (26)–(28) into equations (24) and (25) and using the harmonic balance method yield the following set of algebraic equations in H_{0r}, H_{1r}, I_{0r}, and I_{1r} for the rth vibration mode

$$-(1+\mu_r)\omega^2 H_{0r} + \left(2\zeta_r\omega_r + \frac{8}{3\pi}\gamma_r\omega\sqrt{H_{0r}^2 + H_{1r}^2}\right) \times \omega H_{1r} + \omega_r^2 H_{0r} - \theta_r V = 0, \tag{29}$$

$$-(1+\mu_r)\omega^2 H_{1r} - \left(2\zeta_r\omega_r + \frac{8}{3\pi}\gamma_r\omega\sqrt{H_{0r}^2 + H_{1r}^2}\right) \times \omega H_{0r} + \omega_r^2 H_{1r} = 0, \tag{30}$$

$$-I_{0r} + \theta_r\omega H_{1r} = 0, \tag{31}$$

$$I_{1r} + C^{\mathrm{eq}}\omega + \theta_r\omega H_{0r} = 0. \tag{32}$$

The following simplification suggested by Sarpkaya [45], and later used by Aureli *et al* [34] and Cha *et al* [31], is employed for the nonlinear damping term:

$$|\hat{H}\mathrm{Im}[e^{j\omega t}]|\hat{H}\mathrm{Im}[e^{j\omega t}] = \frac{8}{3\pi}|\hat{H}|\hat{H}\mathrm{Im}[e^{j\omega t}], \tag{33}$$

where $\hat{H}$ is a complex number. The resulting system of algebraic equations is solved numerically using the solve function in MATLAB.

3. Experimental validations

Three MFC bimorphs shown in figure 4(a) are tested and characterized in air and under water using the clamps employed for in-air actuation FRF measurements. Each bimorph is made from two identical custom-made MFC laminates (sufficiently hydrophobic due to custom-made polyester electrode sheets) labeled as M8507-P1, M8514-P1 and M8528-P1 (figure 4(a)) by Smart Material Corp. The piezoelectric laminates are assembled by using high shear strength epoxy through vacuum bonding process described elsewhere [59]. The electrode leads of the MFC bimorphs are connected in parallel throughout the experiments discussed in this paper. The bimorphs are cantilevered in aluminum clamps with the basic geometry and structural properties given in table 2.

A sample bimorph (M8514-P1) cantilever in its fixture mounted rigidly on to an optical table is shown in figure 4(b) for in-air actuation test. During actuation experiments, the actuation voltage signal (harmonic excitation with 10 averages) is generated by a Spectral Dynamics SigLab data acquisition device while a Trek high voltage amplifier (Trek, inc. Model 2220) provides reference driving voltage and monitors current as well. A laser doppler vibrometer (LDV, Polytec PDV 100) is used along with the monitored actuation signal to obtain the tip velocity and admittance FRFs of the MFC bimorphs in air and under water. Note that the admittance FRF (actuation current-to-voltage ratio) is useful to obtain the actuation power consumption level [60].

Underwater experiments are conducted in the same setup as the in-air case (figure 5(a)) and an LDV is used for

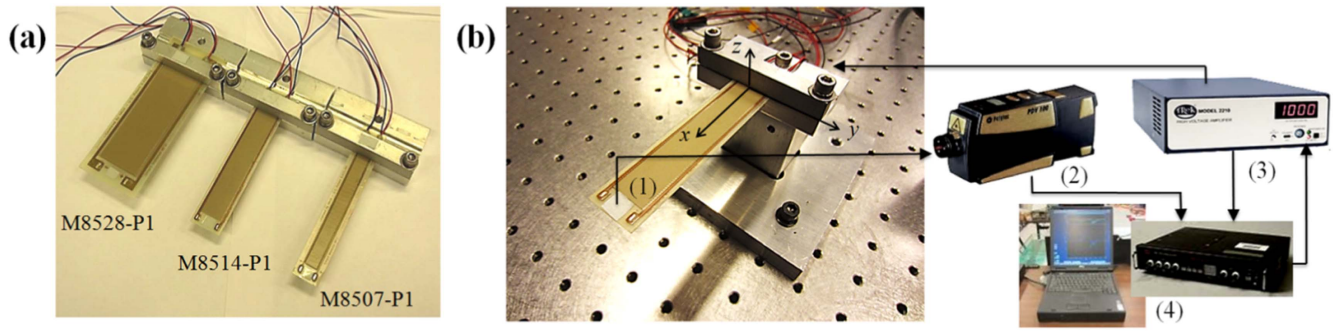

Figure 4. (a) MFC bimorphs in aluminum clamps, and (b) in-air dynamic actuation test setup: (1) sample bimorph (M8514-P1) cantilever in fixture mounted rigidly on to table, (2) LDV for the measurement of the bimorph tip velocity FRF, (3) high voltage amplifier, and (4) data acquisition system.

obtaining the transverse tip velocity under dynamic actuation (figure 5(b)). Note that, the laser signal amplitude is divided by the refractive index of water ($n = 1.333$) in the underwater experiments [24, 25].

3.1. In-air tip velocity and admittance FRFs and parameter identification

Tip velocity and admittance FRFs from in-air actuation experiments and model simulation for the three bimorphs (M8507-P1, M8514-P1, and M8528-P1) are shown in figures 6–8, respectively. The inset figures show close-up views around the resonance frequencies. The identified parameters from in-air actuation experiments are summarized in table 3. Comparing the experimental and analytical second resonance frequency values shows less than 4% error. The major source of inaccuracy is unmolded effects (such as shear effects in the bonding layer) which can be manifested and pronounced in a mode shape-dependent way. Damping ratios for the first and the second mode (ζ_1 and ζ_2) are obtained by using the half-power method [61], electromechanical coupling in physical coordinate (ϑ) is obtained from equation (8) using mixing rules (parallel connection of MFC laminates) for each sample and the equivalent capacitance (C^{eq}) is measured experimentally. Overall the electroelastic model successfully represents the in-air dynamics of the samples for small oscillations as further discussed in the next section by comparing modeled and identified system parameters.

3.2. Analytical versus experimental system parameters

In figure 9, modal electromechanical coupling (θ_r) and piezoelectric constant (e_{33}) of the custom-made piezoelectric MFCs with polyester electrode sheets are measured experimentally and compared with the effective properties obtained from the model employing mixing rules formulation. Details of the geometric and homogeneous properties of the active (PZT fibers) and passive (epoxy) layers of MFCs can be found in [47]. From the surface image (e.g. figure 2(b) for M8514-P1 bimorph) the width of each piezoceramic fiber is approximately 355.5 μm and each epoxy layer between the fibers has a width of 34.4 μm. Since the total active width is

Table 2. Geometric and structural properties of the MFC bimorphs (L is the overhang length, b is the width, h is the total thickness and m_s is the structural mass per length). The active length and width define the portions which include the piezoelectric fibers.

	L (mm) (Active, overall)	b (mm) (Active, overall)	h (mm)	m_s (kg m^{-1})
M8507-P1	[75.5, 83.5]	[7, 16.5]	0.61	0.028
M8514-P1	[75.5, 83.5]	[14, 21.5]	0.61	0.045
M8528-P1	[75.5, 88.5]	[28, 43.5]	0.61	0.090

14 mm, this sample (M8514-P1) has approximately 36 piezoceramic fibers ($M = 36$) and $\nu = 0.9$. The average spacing between two subsequent electrodes is 407.18 μm. Therefore, the number of RVEs over the beam length is 185 ($N = 185$). Having the measured capacitance of the MFCs, the average effective surface area of each RVE , A_e in equations (8) and (9), is calculated as 0.02 mm^2 while h_{pc} is approximately 157 μm.

The MFCs use Navy II piezoceramics, for which the effective value of the piezoelectric constant for RVE is $e_{33,e} = 19.1$ C m^{-2}. In table 4, properties of PZT fibers, epoxy, RVE (the equivalent properties for RVE are calculated by mixing rules), and MFC are given. It is important to note that, as shown in figures 1 and 2, the electrode layers are made from epoxy and copper fibers (volume fraction of copper is approximately 24%) which are perpendicular to the PZT fibers while the composite structure is embedded in Kapton film. The in-plane (yz-plane) sequence of layers for an MFC is shown in detail by Deraemaeker *et al* [49] and Shahab and Erturk [47]. The equivalent properties of electrode-Kapton layer are calculated using the mixing rules. Then the properties of an MFC are calculated from the properties of all the included layers (PZT-epoxy and electrode-Kapton layers). For example, each RVE has the equivalent Young's modulus as 48.3 GPa, by including the electrode-Kapton layers (c_{33}^E is 117.2 GPa and 2.8 GPa for copper and Kapton, respectively), c_{33}^E is evaluated as 31.1 GPa and the piezoelectric constant is $e_{33} = 13.6$ C m^{-2} for MFC. The reported values in table 4 compare favorably with the previously published numerical

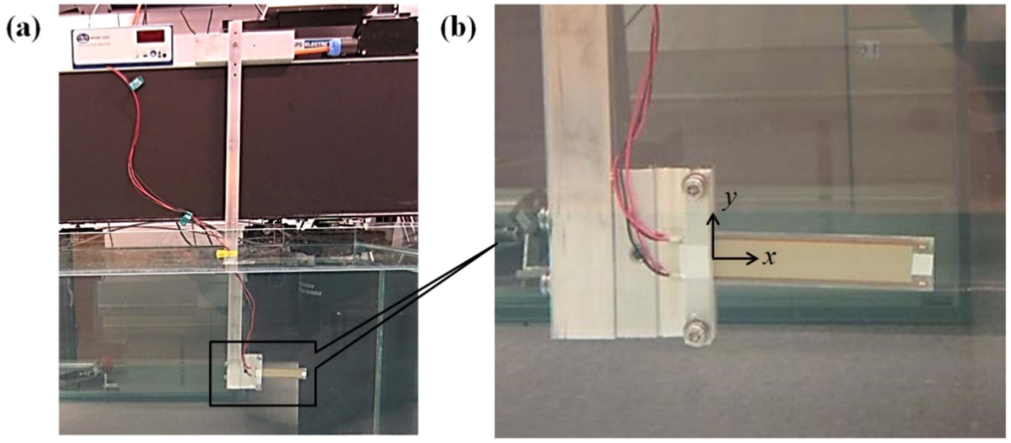

Figure 5. (a) Underwater configuration of the bimorph MFC cantilever for the measurement of its tip velocity FRF and (b) close-up view of a clamped M8514-P1 type bimorph cantilever fixed to the aluminum bar.

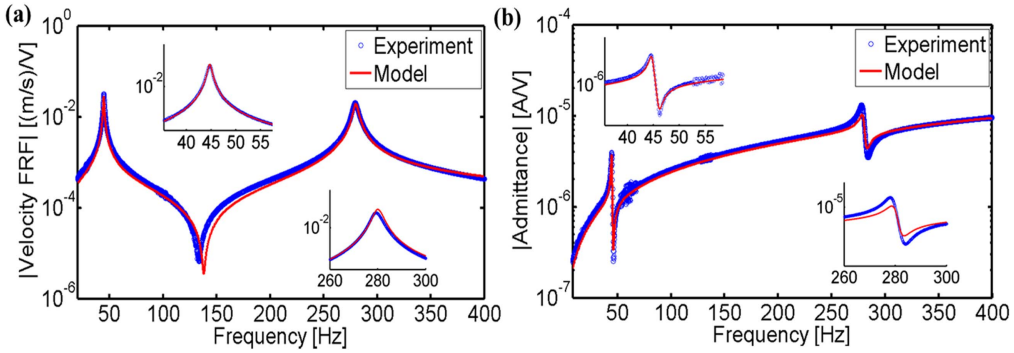

Figure 6. Experimental and analytical results for in-air actuation of M8507-P1 bimorph cantilever: (a) tip velocity and (b) admittance FRFs.

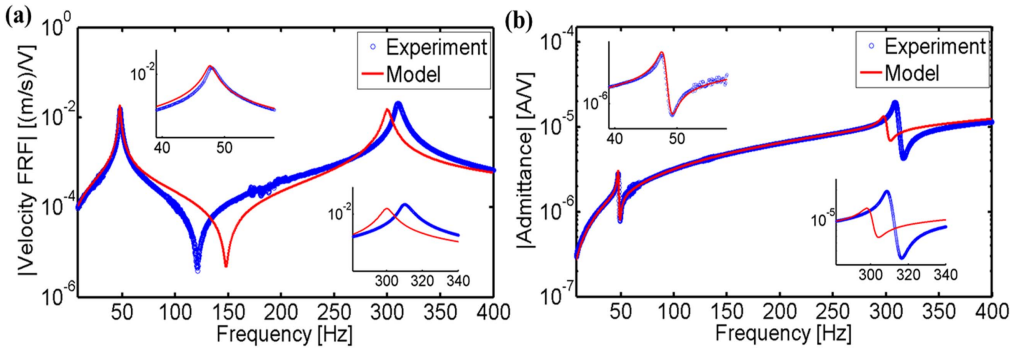

Figure 7. Experimental and analytical results for in-air actuation of M8514-P1 bimorph cantilever: (a) tip velocity and (b) admittance FRFs.

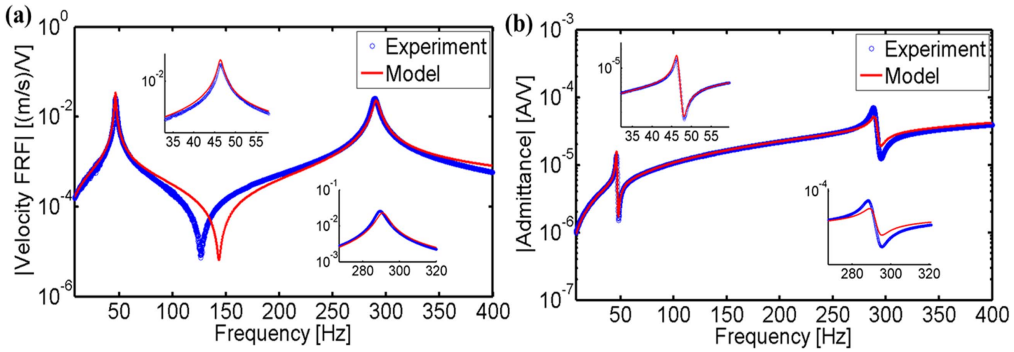

Figure 8. Experimental and analytical results for in-air actuation of M8528-P1 bimorph cantilever: (a) tip velocity and (b) admittance FRFs.

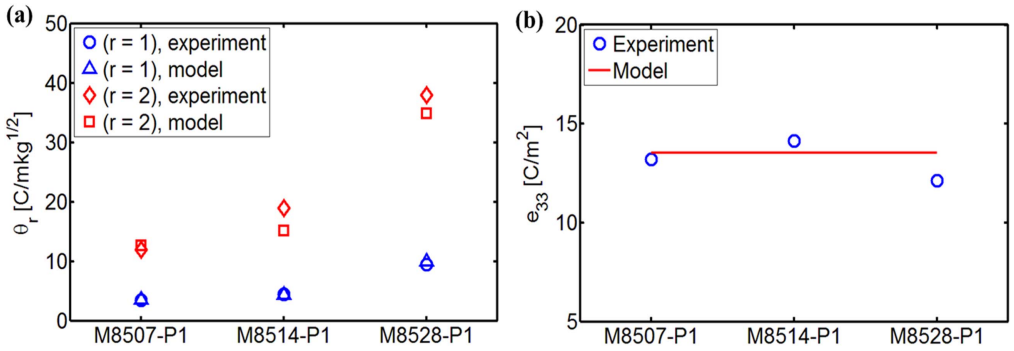

Figure 9. Experimental and analytical results for (a) modal electromechanical coupling, θ_r, and (b) equivalent piezoelectric constant, e_{33}.

Table 3. Identified parameters from in-air actuation experiments (f_2 is given in the form of [experimental, analytical] and $f_r = \omega_r/2\pi$).

	M8507-P1	M8514-P1	M8528-P1
f_1 (Hz)	44.7	47.9	46.4
f_2 (Hz)	[279.3, 280.1]	[309.8, 300.2]	[289.2, 290.8]
D (N m^2)	0.0058	0.0107	0.0201
ζ_1, ζ_2 (%)	1.8, 1.5	2, 1.5	1.5, 1.2
ϑ (10^{-6} Nm V^{-1})	4.53	6.89	22.73
C^{eq} (nF)	3.8	5.5	17.5

Table 4. Properties of active layer (PZT fiber), passive layer or matrix (epoxy), RVE, and 33-mode MFCs using analytical mixing rules ($\varepsilon_0 = 8.854$ pF m^{-1} is the permittivity of free space, $\varepsilon_{33}^S = \varepsilon_{33}^T - d_{33}^2 c_{33}^E$).

	PZT fiber	Epoxy	RVE	MFC
c_{33}^E (GPa)	48.30	3.10	43.78	31.10
d_{33} (pm V^{-1})	440	—	437	437
$\varepsilon_{33}^T/\varepsilon_0$	1850	4.25	1665	1665
ε_{33}^S (nF m^{-1})	7.02	—	6.38	8.8

and experimental data as well as the data from the manufacturer [49, 62].

It is possible to use the experimental results for parameter identification, as done in figure 9 for the piezoelectric constant. A good agreement is observed between the theoretical predictions and experimental results in figure 9. In addition, the results are consistent with the empirical estimates given by Cacan and Erturk [63] for standard MFCs. This approach therefore fully bridges the effective electroelastic, elastic, and dielectric properties of the MFCs and the global electroelastic dynamics of the MFC laminates explored in this work for actuation.

3.3. Underwater velocity and admittance FRFs

Having validated the analytical model results for in-air actuation of the bimorphs and identified parameters, three case studies are tested and analyzed for underwater actuation. As displayed in figure 5, each MFC bimorph is submerged in quiescent water along with the same aluminum clamp used for in-air experiments.

Figures 10–12 show the experimental and semi-empirical model (using Morison hydrodynamic function) tip velocity and admittance FRFs for a frequency range of 12–130 Hz which captures underwater first two bending mode frequencies of the bimorphs. The inertia and drag coefficients, c_m and c_d, are obtained by the analysis done on purely experimental in-air and underwater data to avoid interference of other measurement and modeling errors (see the appendix). Then c_m and c_d are used in the analytical model to give figures 10–12. In table 5, the experimental underwater fundamental frequencies and total damping ratios are listed (ζ_T in table 5 includes structural damping ratio and the added fluid damping). As expected, the effect of fluid loading is to lower the resonance frequencies of the MFCs (for both modes) and to increase the damping ratio as compared to in-air actuation results reported in table 3. The electromechanical coupling term, ϑ, in each case is the same as the ones obtained from the in-air experiment.

3.4. Analysis of hydrodynamic inertia and drag coefficients

Figures 13(a)–(d) display the identified hydrodynamic inertia and drag coefficients (c_m and c_d in Morison's hydrodynamic function) focusing on the first two bending modes for both base-excited aluminum and actuated MFC cantilevers with different aspect ratios ($\psi = \mathrm{L/b}$). Experimental vibration characteristics of the aluminum strips considered in this study are explained in detail by Shahab and Erturk [64]. It is observed that the inertia and drag coefficients show asymptotic behavior for ψ greater than approximately 5, making inertia and drag coefficients insensitive to ψ ratio (cases of ψ smaller than 5 are sensitive to aspect ratio). Specifically, In figures 13(a) and (b), $c_m(\psi)$ value converges to unity (for large ψ) in agreement with the predictions of classical flow solutions based on 2D fluid-structure problem in which linear hydrodynamic forces are dominant [26, 65]. In figures 13(c) and (d), $c_d(\psi)$ approaches the values close to 21 and 125 for the first and second vibration modes, respectively, consistent with the range of experimental and numerical data summarized in figure 11 of Kopman and Porfiri [41].

Figure 13 shows the asymptotic increase of c_m and c_d with increased ψ for each mode separately. The curve fitting

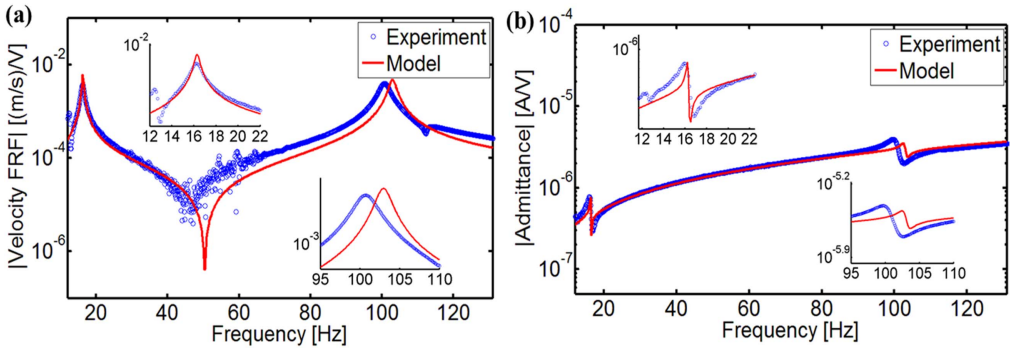

Figure 10. Experimental and analytical results for underwater actuation of bimorph M8507-P1 cantilever: (a) tip velocity and (b) admittance FRFs.

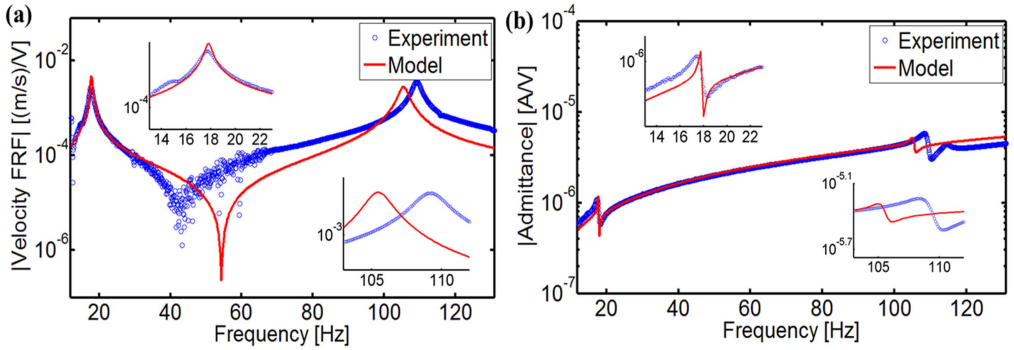

Figure 11. Experimental and analytical results for underwater actuation of bimorph M8514-P1 cantilever: (a) tip velocity and (b) admittance FRFs.

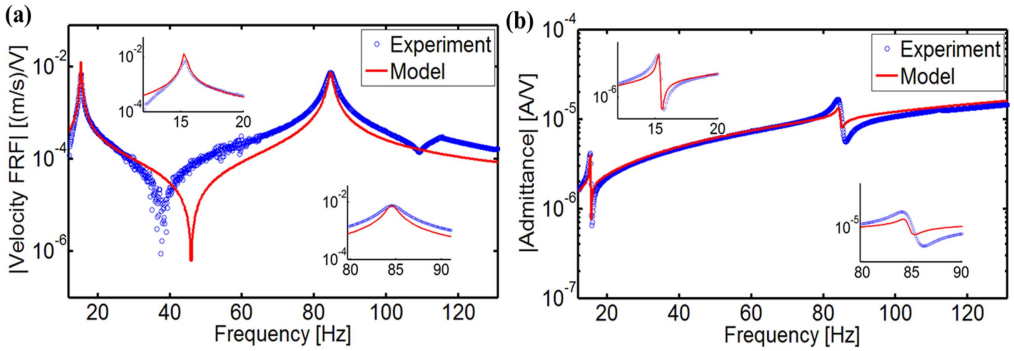

Figure 12. Experimental and analytical results for underwater actuation of bimorph M8528-P1 cantilever: (a) tip velocity and (b) admittance FRFs.

Table 5. Experimentally identified model parameters from underwater tests.

	M8507-P1	M8514-P1	M8528-P1
f_1 (Hz)	15.9	17.5	15.2
f_2 (Hz)[a]	[100.7, 103]	[109.2, 105.5]	[84.6, 84.5]
ζ_{T_1}, ζ_{T_2} (%)	3.3, 2.5	4.3, 3.2	3.3, 2.4

[a] f_2 is given in the form of [experimental, analytical].

toolbox of MATLAB is used in order to represent the curves given in figure 13. The following quadratic curve fit polynomial ratio expressions are given for the dimensionless inertia and drag coefficients focusing on the two first bending modes:

$$\begin{aligned} c_{m1} &= \frac{\psi^2 - 0.701\psi + 0.3745}{\psi^2 - 1.111\psi + 2.637}, \\ c_{m2} &= \frac{\psi^2 + 6.99\psi - 1.658}{\psi^2 + 5.36\psi + 11.46} \\ c_{d1} &= \frac{\psi^2 + 0.1432\psi + 0.5618}{0.04983\psi^2 - 0.03946\psi + 0.2674}, \\ c_{d2} &= \frac{\psi^2 - 0.412\psi + 0.4096}{0.008492\psi^2 - 0.007883\psi + 0.01853}. \end{aligned} \tag{34}$$

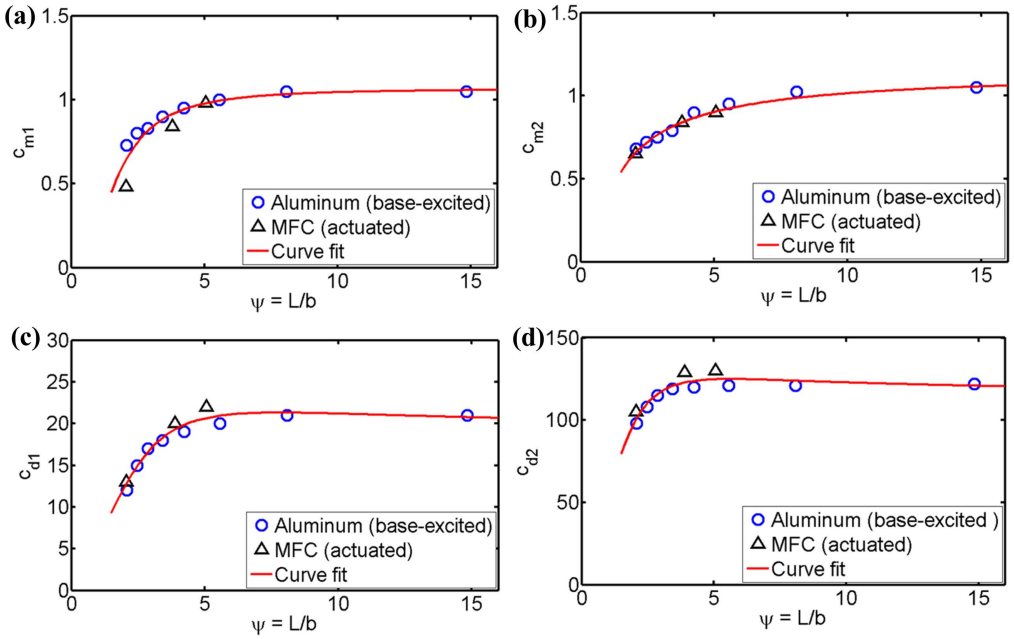

Figure 13. Hydrodynamic inertia coefficient (c_m) versus aspect ratio (ψ) for (a) mode 1 and (b) mode 2; hydrodynamic drag coefficient (c_d) versus ψ for (c) mode 1 and (d) mode 2.

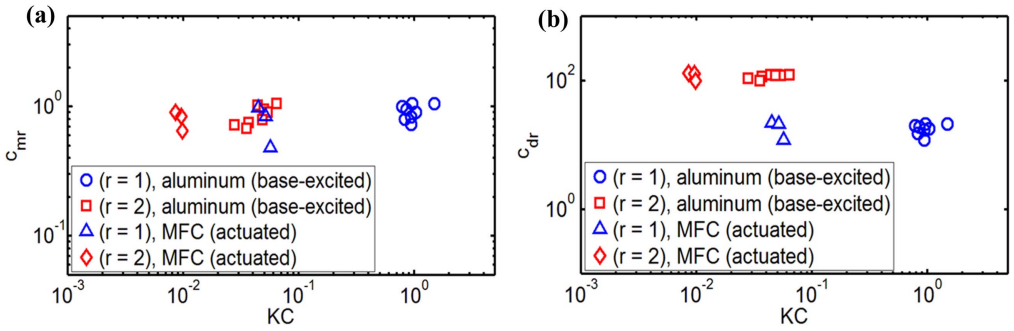

Figure 14. (a) Hydrodynamic inertia coefficient (c_{mr}) and (b) drag coefficient (c_{dr}) versus KC number for the first two vibration modes.

Comparing c_m and c_d values that belong to the first and the second modes in figure 13 shows that both aspect ratio and vibration frequency (especially for drag coefficient) are determinants of fluid loading effects. The frequency dependence is implicitly involved in the dependence of the inertia and drag coefficients on the KC number, or the period number: $\mathrm{KC} = 2\pi\ |w(L)|/b$ where $|w(L)|$ is the maximum tip displacement amplitude of the oscillating beam. Figure 14 displays the identified hydrodynamic inertia and drag coefficients versus KC for both aluminum and MFC cantilevers with different aspect ratios. The underwater vibration characteristics of aluminum strips (Shahab and Erturk [64]) and MFCs show that resonance frequencies of these two groups keep close values for the same aspect ratio. Note that the maximum displacement amplitudes for base-excited aluminum cantilevers are larger than the MFC ones. Therefore, the results for the aluminum samples in figure 14 are given for larger KC numbers. Figure 14(a) shows that, for both aluminum and MFC samples, the inertia coefficients for the first and the second modes are on the same order of magnitude (tend to converge to unity with increased aspect ratio), making them relatively insensitive to vibration frequency and amplitude for the KC range in this study ($0.008 < \mathrm{KC} < 1.5$). For each mode, the aluminum and the MFC samples give drag coefficients on the same order of magnitude (figure 14(b)). In contrast to the behavior of inertia coefficient, for a given sample (MFC or aluminum) the drag coefficient shows great sensitivity to vibration mode, which suggests the presence of a mode shape dependence for the drag coefficient. However, for a given vibration mode, the drag coefficient for different samples (MFC versus aluminum) is on the same order of magnitude.

4. Conclusions

Thin cantilevers made from MFC bimorphs of different aspect ratios can be employed for underwater actuation, sensing, and power generation, among other aquatic applications of direct and converse piezoelectric effects. In an effort to develop electrohydroelastic models for such cantilevers, the present work investigated MFC bimorphs with

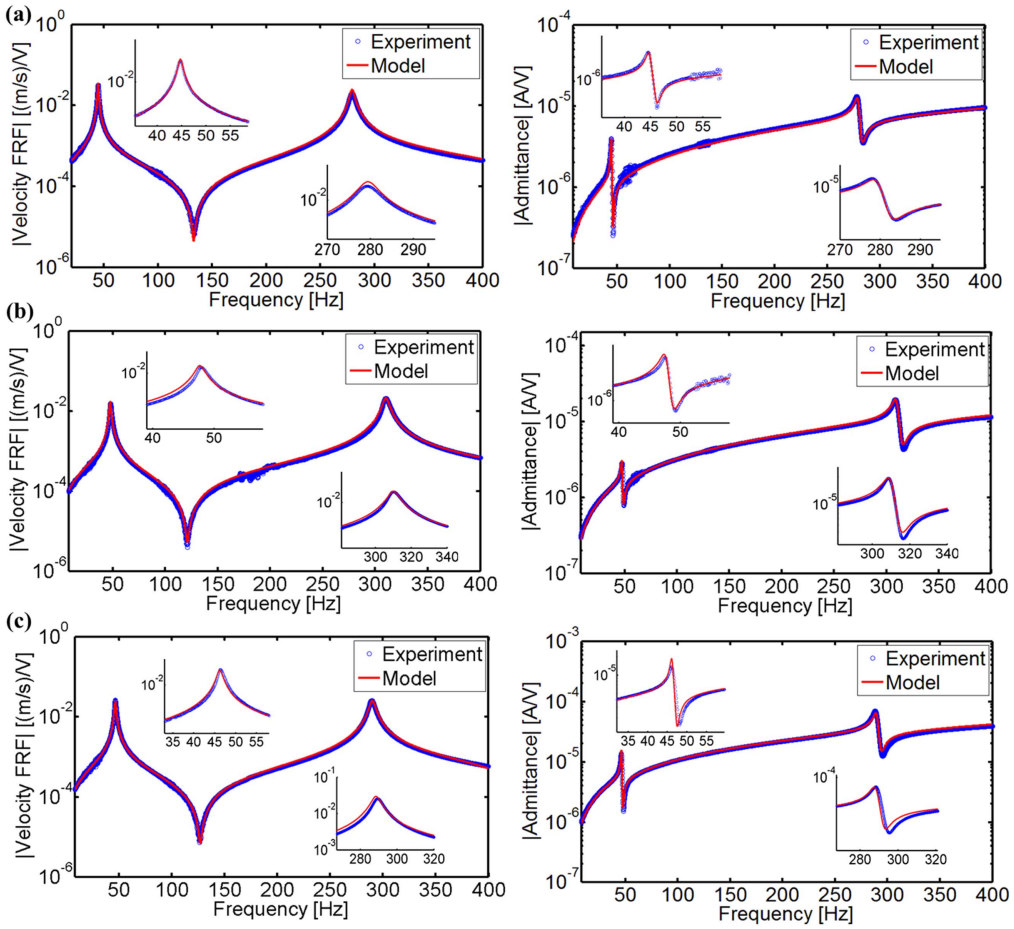

Figure A1. In-air experimental and model frequency response results for actuation: tip velocity (left) and admittance FRFs (right) for (a) M8507-P1, (b) M8514-P1 and (c) M8528-P1.

three different aspect ratios under dynamic actuation. Mixing rules-based (i.e. rule of mixtures) electroelastic mechanics formulation was coupled with the global electroelastic dynamics based on the Euler–Bernoulli kinematics which was then coupled with Morison's semi-empirical model to account for aspect ratio dependent nonlinear hydrodynamic effects. The tip velocity and admittance FRFs were successfully modeled for in-air actuation and validated experimentally for all aspect ratios considered herein. Underwater tip velocity and admittance FRFs were then derived by combining their in-air counterparts with Morison's nonlinear hydrodynamic function. The inertia and drag coefficients in Morison's equation were identified experimentally and compared with the ones obtained from base-excited aluminum cantilevers of similar aspect ratios. In addition to the smooth trend and converging behavior of the inertia and drag coefficients with increased aspect ratio, the agreement between the MFC and aluminum cantilever test results for both vibration modes was reported. The repeatability of the inertia and drag coefficients in Morison's equation was noted to be promising for samples with the same aspect ratio. The inertia and drag coefficients were also explored against the KC number. The drag coefficient was observed to be more sensitive to the vibration mode J;(first mode versus second mode in bending) for a given sample. Overall the semi-empirical Euler–Bernoulli–Morison model presented here can be used conveniently for predicting the underwater dynamics of piezoelectric cantilevers for geometrically and materially linear behavior.

Acknowledgments

This work was supported in part by the National Science Foundation under Grant CMMI-1254262.

Appendix

Experimentally measured in-air and underwater FRFs (figures A1 and A2) are correlated to accurately identify the inertia and drag coefficients for the first two modes. That is, purely experimental structural (in air—approximately in vacuo for infinitesimal oscillations) natural frequencies and structural damping ratios are used in the model FRF in figure A1. Then, the modal inertia and drag coefficients are identified using this experiment-based model to have the model versus experiment agreement in figure A2.

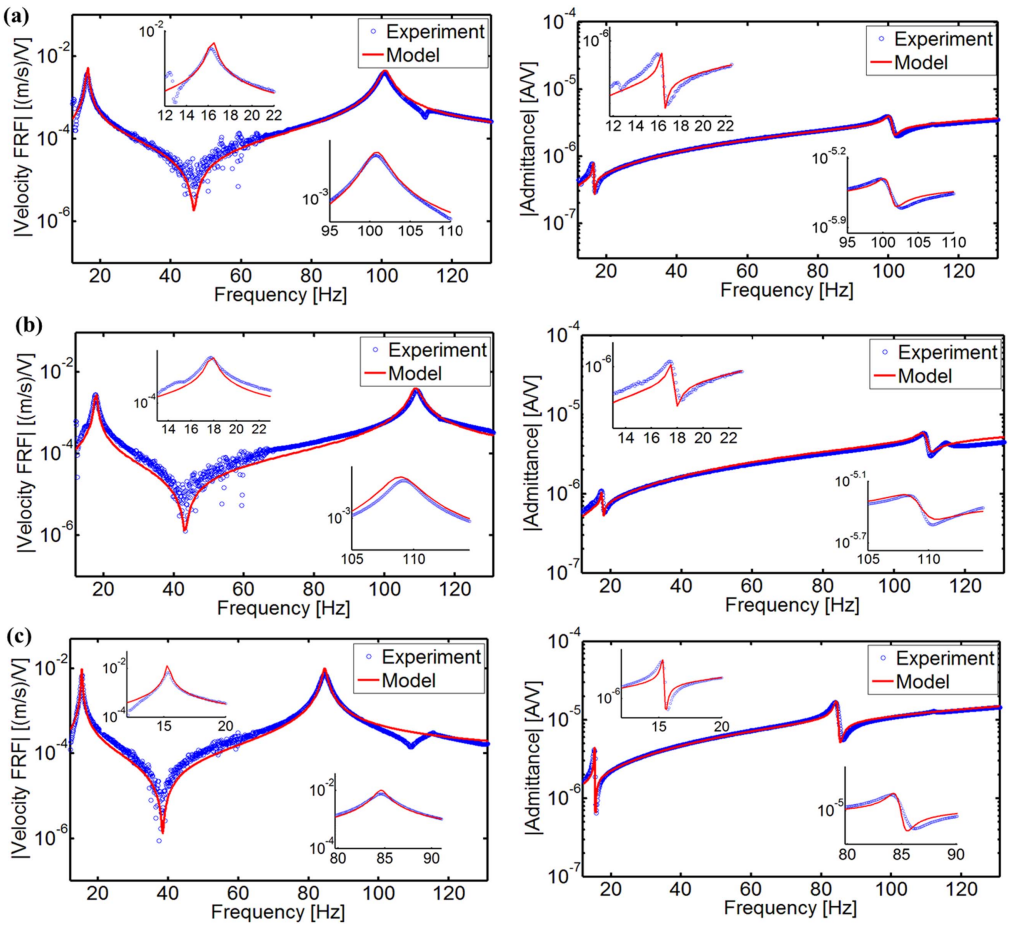

Figure A2. Underwater experimental and model frequency response results for actuation: tip velocity (left) and admittance FRFs (right) for (a) M8507-P1, (b) M8514-P1 and (c) M8528-P1.

References

[1] Bandyopadhyay P R 2005 Trends in biorobotic autonomous undersea vehicles *IEEE J. Ocean. Eng.* **30** 109–39

[2] Chu W-S *et al* 2012 Review of biomimetic underwater robots using smart actuators *Int. J. Precis. Eng. Manuf.* **13** 1281–92

[3] Roper D *et al* 2011 A review of developments towards biologically inspired propulsion systems for autonomous underwater vehicles *Proc. Inst. Mech. Eng.* M **225** 77–96

[4] Liu F, Lee K-M and Yang C-J 2012 Hydrodynamics of an undulating fin for a wave-like locomotion system design *IEEE/ASME Trans. Mechatronics* **17** 554–62

[5] Liu J, Dukes I and Hu H 2005 Novel mechatronics design for a robotic fish *IEEE/RSJ Int. Conf. on Intelligent Robots and Systems* (Piscataway, NJ: IEEE)

[6] Wen L *et al* 2013 Quantitative thrust efficiency of a self-propulsive robotic fish: experimental method and hydrodynamic investigation *IEEE/ASME Trans. Mechatronics* **18** 1027–38

[7] Zhou C and Low K 2012 Design and locomotion control of a biomimetic underwater vehicle with fin propulsion *IEEE/ASME Trans. Mechatronics* **17** 25–35

[8] Crespi A *et al* 2008 Controlling swimming and crawling in a fish robot using a central pattern generator *Auton. Robots* **25** 3–13

[9] Kim B *et al* 2005 A biomimetic undulatory tadpole robot using ionic polymer–metal composite actuators *Smart Mater. Struct.* **14** 1579

[10] Tan X B *et al* 2006 An autonomous robotic fish for mobile sensing *IEEE/RSJ Int. Conf. on Intelligent Robots and Systems* vols 1–12 2006 pp 5424–9

[11] Ye X, Su Y and Guo S 2007 A centimeter-scale autonomous robotic fish actuated by IPMC actuator *IEEE Int. Conf. on Robotics and Biomimetics, 2007. ROBIO 2007* (Piscataway, NJ: IEEE)

[12] Ye X *et al* 2008 Design and realization of a remote control centimeter-scale robotic fish *IEEE/ASME Int. Conf. on Advanced Intelligent Mechatronics* (Piscataway, NJ: IEEE)

[13] Mbemmo E *et al* 2008 Modeling of biomimetic robotic fish propelled by an ionic polymer-metal composite actuator *IEEE Int. Conf. on Robotics and Automation. 2008 ICRA 2008* (Piscataway, NJ: IEEE)

[14] Aureli M, Kopman V and Porfiri M 2010 Free-locomotion of underwater vehicles actuated by ionic polymer metal composites *IEEE/ASME Trans. Mechatronics* **15** 603–14

[15] Chen Z, Shatara S and Tan X 2010 Modeling of biomimetic robotic fish propelled by an ionic polymer–metal composite caudal fin *IEEE/ASME Trans. Mechatronics* **15** 448–59

[16] Aureli M and Porfiri M 2010 Low frequency and large amplitude oscillations of cantilevers in viscous fluids *Appl. Phys. Lett.* **96** 164102

[17] Wilkie W K *et al* 2000 Low-cost piezocomposite actuator for structural control applications *SPIE's 7th Annual Int. Symp. on Smart Structures and Materials* (International Society for Optics and Photonics)

[18] Bryant R G 2007 *Overview of NASA Langley's Piezoelectric Ceramic Packaging Technology and Applications* (Langley Research Center: National Aeronautics and Space Administration)

[19] Bent A A 1997 *Active Fiber Composites for Structural Actuation* (Ph.D. Thesis, Massachusetts Institute of Technology, Boston, MA)

[20] Nagata Y *et al* 2008 Development of underwater robot using macro fiber composite *IEEE/ASME Int. Conf. on Advanced Intelligent Mechatronics, 2008 AIM 2008* (Piscataway, NJ: IEEE)

[21] Ming A *et al* 2009 Development of underwater robots using piezoelectric fiber composite *IEEE Int. Conf. on Robotics and Automation 2009 ICRA'09* (Piscataway, NJ: IEEE)

[22] Shintake J, Ming A and Shimojo M 2010 Development of flexible underwater robots with caudal fin propulsion *2010 IEEE/RSJ Int. Conf. on Intelligent Robots and Systems (IROS)* (Piscataway, NJ: IEEE)

[23] Kancharala A and Philen M 2014 Enhanced hydrodynamic performance of flexible fins using macro fiber composite actuators *Smart Mater. Struct.* **23** 115012

[24] Erturk A and Delporte G 2011 Underwater thrust and power generation using flexible piezoelectric composites: an experimental investigation toward self-powered swimmer-sensor platforms *Smart Mater. Struct.* **20** 125013

[25] Cen L and Erturk A 2013 Bio-inspired aquatic robotics by untethered piezohydroelastic actuation *Bioinsp. Biomim.* **8** 016006

[26] Sader J E 1998 Frequency response of cantilever beams immersed in viscous fluids with applications to the atomic force microscope *J. Appl. Phys.* **84** 64–76

[27] Chon J W, Mulvaney P and Sader J E 2000 Experimental validation of theoretical models for the frequency response of atomic force microscope cantilever beams immersed in fluids *J. Appl. Phys.* **87** 3978–88

[28] Van Eysden C A and Sader J E 2006 Resonant frequencies of a rectangular cantilever beam immersed in a fluid *J. Appl. Phys.* **100** 114916

[29] Van Eysden C A and Sader J E 2007 Frequency response of cantilever beams immersed in viscous fluids with applications to the atomic force microscope: arbitrary mode order *J. Appl. Phys.* **101** 044908

[30] Brunetto P *et al* 2008 A model of ionic polymer–metal composite actuators in underwater operations *Smart Mater. Struct.* **17** 025029

[31] Cha Y, Kim H and Porfiri M 2013 Energy harvesting from underwater base excitation of a piezoelectric composite beam *Smart Mater. Struct.* **22** 115026

[32] Aureli M *et al* 2010 Energy harvesting from base excitation of ionic polymer metal composites in fluid environments *Smart Mater. Struct.* **19** 015003

[33] Tuck E O 1969 Calculation of unsteady flows due to small motions of cylinders in a viscous fluid *J. Eng. Math.* **3** 29–44

[34] Aureli M, Basaran M and Porfiri M 2012 Nonlinear finite amplitude vibrations of sharp-edged beams in viscous fluids *J. Sound Vib.* **331** 1624–54

[35] Falcucci G *et al* 2011 Transverse harmonic oscillations of laminae in viscous fluids: a lattice Boltzmann study *Phil. Trans. R. Soc.* A **369** 2456–66

[36] Phan C N, Aureli M and Porfiri M 2013 Finite amplitude vibrations of cantilevers of rectangular cross sections in viscous fluids *J. Fluids Struct.* **40** 52–69

[37] Tafuni A and Sahin I 2014 Nonlinear hydrodynamics of thin laminae undergoing large harmonic oscillations in a viscous fluid *J. Fluids Struct.* **52** 101–11

[38] Facci A L and Porfiri M 2013 Analysis of three-dimensional effects in oscillating cantilevers immersed in viscous fluids *J. Fluids Struct.* **38** 205–22

[39] Bidkar R A *et al* 2009 Nonlinear aerodynamic damping of sharp-edged flexible beams oscillating at low Keulegan–Carpenter numbers *J. Fluid Mech.* **634** 269–89

[40] Choi M, Cierpka C and Kim Y-H 2012 Vortex formation by a vibrating cantilever *J. Fluids Struct.* **31** 67–78

[41] Kopman V and Porfiri M 2013 Design, modeling, and characterization of a miniature robotic fish for research and education in biomimetics and bioinspiration *IEEE/ASME Trans. Mechatronics* **18** 471–83

[42] Morison J, Johnson J and Schaaf S 1950 The force exerted by surface waves on piles *J. Pet. Technol.* **2** 149–54

[43] Morison J, Johnson J W and O'Brien M P 1953 Experimental studies of forces on piles *Coast. Eng. Proc.* **1** 25

[44] Graham J M R 1980 The forces on sharp-edged cylinders in oscillatory flow at low Keulegan–Carpenter numbers *J. Fluid Mech.* **97** 331–46

[45] Sarpkaya T 1986 Force on a circular cylinder in viscous oscillatory flow at low Keulegan–Carpenter numbers *J. Fluid Mech.* **165** 61–71

[46] Shahab S and Erturk A 2015 Experimentally validated nonlinear electrohydroelastic Euler–Bernoulli–Morison model for macro-fiber composites with different aspect ratios *ASME 2015 Int. Design Engineering Technical Conf. and Computers and Information in Engineering Conf.* (American Society of Mechanical Engineers)

[47] Shahab S and Erturk A 2015 Unified electrohydroelastic investigation of underwater energy harvesting and dynamic actuation by incorporating Morison's equation *SPIE Smart Structures and Materials + Nondestructive Evaluation and Health Monitoring* (International Society for Optics and Photonics)

[48] Keulegan G H and Carpenter L H 1956 *Orces on Cylinders and Plates in an Oscillating Fluid* (US Department of Commerce, National Bureau of Standards)

[49] Deraemaeker A *et al* 2009 Mixing rules for the piezoelectric properties of macro fiber composites *J. Intell. Mater. Syst. Struct.* **20** 1475–82

[50] Agarwal B D, Broutman L J and Chandrashekhara K 2006 *Analysis and Performance of Fiber Composites* (New York: Wiley)

[51] Erturk A and Inman D J 2008 A distributed parameter electromechanical model for cantilevered piezoelectric energy harvesters *J. Vib. Acoust.* **130** 041002

[52] Erturk A and Inman D J 2009 An experimentally validated bimorph cantilever model for piezoelectric energy harvesting from base excitations *Smart Mater. Struct.* **18** 025009

[53] Erturk A and Inman D J 2011 *Piezoelectric Energy Harvesting* (Chichester: Wiley)

[54] Kundert K S and Sangiovanni-Vincentelli A 1986 Simulation of nonlinear circuits in the frequency domain *IEEE Trans. Comput.-Aided Des. Integr. Circuits Syst.* **5** 521–35

[55] Nayfeh A H 2008 *Perturbation Methods* (New York: Wiley)

[56] Leadenham S and Erturk A 2014 M-shaped asymmetric nonlinear oscillator for broadband vibration energy harvesting: harmonic balance analysis and experimental validation *J. Sound Vib.* **333** 6209–23

[57] Leadenham S and Erturk A 2015 Unified nonlinear electroelastic dynamics of a bimorph piezoelectric cantilever for energy harvesting, sensing, and actuation *Nonlinear Dyn.* **79** 1727–43

[58] Leadenham S and Erturk A 2015 Nonlinear M-shaped broadband piezoelectric energy harvester for very low base accelerations: primary and secondary resonances *Smart Mater. Struct.* **24** 055021

[59] Anton S, Erturk A and Inman D 2010 Multifunctional self-charging structures using piezoceramics and thin-film batteries *Smart Mater. Struct.* **19** 115021

[60] Shahab S, Tan D and Erturk A 2015 Hydrodynamic thrust generation and power consumption investigations for piezoelectric fins with different aspect ratios *Eur. Phys. J. Spec. Top.* **224** 3419–34

[61] Meirovitch L 2010 *Fundamentals of Vibrations* (Long Grove, IL: Waveland Press)

[62] Williams R B 2004 Nonlinear mechanical and actuation characterization of piezoceramic fiber composites *PhD Thesis* Blacksburg (Va), USA

[63] Cacan M and Erturk A 2012 Comparative investigation of the electroelastic dynamics of piezoceramics with interdigitated and uniform electrodes *ASME 2012 Conf. on Smart Materials, Adaptive Structures and Intelligent Systems* (American Society of Mechanical Engineers)

[64] Shahab S and Erturk A 2014 Underwater dynamic actuation of Macro-Fiber Composite flaps with different aspect ratios: electrohydroelastic modeling, testing, and characterization *ASME 2014 Conf. on Smart Materials, Adaptive Structures and Intelligent Systems* (American Society of Mechanical Engineers)

[65] Chu W 1963 *Technical Report* 2 Southwest Research Institute, San Antonio, Texas, DTMB, Contract NObs-86396 (X)